Translational Science

Cancer Research

Genomic Status of *MET* Potentiates Sensitivity to MET and MEK Inhibition in NF1-Related Malignant Peripheral Nerve Sheath Tumors

Jacqueline D. Peacock[1,2], Matthew G. Pridgeon[3], Elizabeth A. Tovar[1], Curt J. Essenburg[1], Megan Bowman[4], Zachary Madaj[4], Julie Koeman[5], Elissa A. Boguslawski[1], Jamie Grit[1], Rebecca D. Dodd[6], Vadim Khachaturov[3], Diana M. Cardona[7], Mark Chen[6], David G. Kirsch[6,8], Flavio Maina[9], Rosanna Dono[9], Mary E. Winn[4], Carrie R. Graveel[1], and Matthew R. Steensma[1,3,10]

Abstract

Malignant peripheral nerve sheath tumors (MPNST) are highly resistant sarcomas that occur in up to 13% of individuals with neurofibromatosis type I (NF1). Genomic analysis of longitudinally collected tumor samples in a case of MPNST disease progression revealed early hemizygous microdeletions in *NF1* and *TP53*, with progressive amplifications of *MET*, *HGF*, and *EGFR*. To examine the role of MET in MPNST progression, we developed mice with enhanced MET expression and *Nf1* ablation ($Nf1^{fl/ko}$;*lox-stop-lox*$MET^{tg/+}$;*Plp-creERT*$^{tg/+}$; referred to as NF1-MET). NF1-MET mice express a robust MPNST phenotype in the absence of additional mutations. A comparison of NF1-MET MPNSTs with MPNSTs derived from $Nf1^{ko/+}$;$p53^{R172H}$;*Plp-creERT*$^{tg/+}$ (NF1-P53) and $Nf1^{ko/+}$;*Plp-creERT*$^{tg/+}$ (NF1) mice revealed unique Met, Ras, and PI3K signaling patterns. NF1-MET MPNSTs were uniformly sensitive to the highly selective MET inhibitor, capmatinib, whereas a heterogeneous response to MET inhibition was observed in NF1-P53 and NF1 MPNSTs. Combination therapy of capmatinib and the MEK inhibitor trametinib resulted in reduced response variability, enhanced suppression of tumor growth, and suppressed RAS/ERK and PI3K/AKT signaling. These results highlight the influence of concurrent genomic alterations on RAS effector signaling and therapy response to tyrosine kinase inhibitors. Moreover, these findings expand our current understanding of the role of MET signaling in MPNST progression and identify a potential therapeutic niche for NF1-related MPNSTs.

Significance: Longitudinal genomic analysis reveals a positive selection for MET and HGF copy number gain early in malignant peripheral nerve sheath tumor progression. *Cancer Res; 78(13); 3672–87. ©2018 AACR.*

Introduction

Neurofibromatosis type I (NF1) is caused by germline mutations in the *NF1* gene and is the most common single-gene disorder affecting approximately 1 in 3,000 live births (1). Approximately 8% to 13% of individuals with NF1 will develop malignant tumors, most commonly malignant peripheral nerve sheath tumors (MPNST). NF1-related MPNSTs are highly aggressive sarcomas that frequently metastasize and have 5-year survival rates ranging from 20% to 50% (2, 3). The mainstay of treatment is surgical resection when possible with consideration of chemotherapy and radiotherapy in select cases. Even though chemotherapy may initially stabilize disease, early responses are typically followed by a rapid evolution of chemoresistance and metastasis (4).

The *NF1* gene encodes neurofibromin, a GTPase-activating protein that regulates RAS (including HRAS, NRAS, and KRAS) and loss of *NF1* leads to deregulated RAS signaling. The RAS signaling node activates multiple kinase effector cascades, including the RAF–MEK–ERK pathway. NF1-related MPNSTs have been shown to arise from *NF1*-null myelinating Schwann cells where neurofibromin deficiency results in RAS deregulation (5, 6). Plexiform neurofibromas are the benign precursors of NF1-related MPNSTs and are formed by a recruited admixture of *NF1* haploinsufficient cells (fibroblasts, mast cells, and perineural cells) following an initial *NF1* loss-of-heterozygosity (LOH) event in a peripheral nerve Schwann cell (7–9).

Several studies implicate oncogenic MET signal activation in NF1-related MPNST disease progression. The oncogene *MET* encodes a receptor tyrosine kinase that is involved in the

[1]Center for Cancer and Cell Biology, Van Andel Research Institute, Grand Rapids, Michigan. [2]College of Health Professions, Ferris State University, Big Rapids, Michigan. [3]Spectrum Health System, Helen DeVos Children's Hospital, Grand Rapids, Michigan. [4]Bioinformatics and Biostatistics Core, Van Andel Research Institute, Grand Rapids, Michigan. [5]Genomics Core, Van Andel Research Institute, Grand Rapids, Michigan. [6]Department of Radiation Oncology, Duke University Medical Center, Durham, North Carolina. [7]Department of Pathology, Duke University Medical Center, Durham, North Carolina. [8]Department Pharmacology and Cancer Biology, Duke University Medical Center, Durham, North Carolina. [9]Aix-Marseille Univ, CNRS, IBDM, Marseille, France. [10]Michigan State University College of Human Medicine, Grand Rapids, Michigan.

Note: Supplementary data for this article are available at Cancer Research Online (http://cancerres.aacrjournals.org/).

J.D. Peacock and M.G. Pridgeon contributed equally to this article.

Current address for R.D. Dodd: Department of Internal Medicine, University of Iowa, Iowa City, Iowa.

Corresponding Author: Matthew R. Steensma, Van Andel Research Institute, 333 Bostwick Ave. NE, Grand Rapids, MI 49503. Phone: 616-234-5378; E-mail: Matt.Steensma@vai.org

doi: 10.1158/0008-5472.CAN-17-3167

progression and metastasis of most solid human cancers (10). The pleiotropic effects of MET activation are mediated through a variety of effector pathways, including dominant regulators of cellular proliferation and survival (i.e., RAS/ERK, PI3K/AKT/mTOR) and cellular motility (STAT3, Rho kinases). MPNSTs often develop from MET-overexpressing plexiform neurofibromas (11). High-resolution array CGH recently identified *MET* and *HGF* gene amplifications in a significant proportion (~30%) of NF1-related MPNSTs (12). MET phosphorylation (Tyr1234/35) was demonstrated in at least half of MPNSTs and was recently proposed as a biomarker for MET-activated MPNSTs (13). In this same study, inhibition of VEGFR2/ MET/RET (cabozantinib) mitigated tumor growth in an MPNST xenograft model. Because genomic alterations in *HGF* and *MET* occur on a backdrop of putative RAS deregulation from germline loss of *NF1* in the stroma, and *NF1* LOH events in the MPNST cell of origin, it is possible that RAS and MET cross-talk contributes to therapy resistance. Toward this end, MET has already been implicated in resistance to RAS pathway inhibition in several cancers, including melanoma and colorectal cancer (14, 15). Although we suspect that RAS/ERK and MET/HGF cooperate to promote cancer progression and therapy resistance, the mechanisms that mediate these complex signaling interactions are not well understood. Recent studies support the concept that cooperative RAS–MET signaling is influenced by genomic alterations within the MET and RAS signaling pathways. Currently, it is unclear (i) whether MET activation is sufficient for malignant transformation of *NF1*-deficient Schwann cells to into MPNSTs and (ii) how the RAS and MET signaling pathways interact in NF1-deficient MPNSTs. Here, we performed a longitudinal genomic analysis to identify key genetic events underlying the transformation of a human plexiform neurofibroma to a MPNST. Our results indicate that *MET* and *HGF* copy number gains were present at the time of MPNST diagnosis and increased during disease progression and treatment. In addition to *MET* and *HGF* copy number variations, the NF1-related MPNST exhibited highly complex genomic structural variations that evolved over time, leading to additional genomic gains and losses that appear to be nonrandom and adaptive for MPNST progression (16, 17).

To further interrogate the role of MET signaling in MPNST progression and therapy response, we developed and characterized a unique mouse model of MET activation in *p53* wild-type, *Nf1*-null myelinating cells. Our hypothesis is that MET activation is sufficient to drive malignant tumorigenesis when combined with putative *NF1* loss of function, and that MET-activated MPNSTs will respond to targeted MET inhibition. Our findings build upon prior work examining *NF1* LOH in myelinating cells (18, 19) and present a complementary model of MPNST to established models combining *Nf1* loss with *p53* or *Ink4a/Arf* (20, 21). Our results demonstrate that highly selective MET inhibition is effective against MPNSTs bearing a "MET addicted" signature, whereby MET inhibition also mitigates downstream RAS–ERK and PI3K–AKT activation. Conversely, we show reduced effectiveness of MET inhibitor monotherapy in *Met*-amplified, *p53*-deficient ("NF1-P53") NF1-related MPNSTs. These findings are attributable in part to signaling adaptations that occur early during therapy that may be affected by loss of P53 function. To address our hypothesis regarding RAS–MET signaling and therapy resistance in NF1-related MPNSTs, we also show that the combination of capmatinib (INCB28060; Novartis; MET inhibitor) and trametinib (Novartis; GSK1120212; MEK inhibitor) results in enhanced therapy effectiveness and reduced tumor response variation compared with monotherapy. Combined capmatinib and trametinib treatment was the most effective treatment in decreasing ERK, AKT, and MET activity in tumorgrafts. These results expand our current understanding of the role of RAS–MET signaling in MPNST disease progression and identify a potential therapeutic niche for NF1-related MPNSTs. Moreover, these findings highlight the influence of cooccurring genomic alterations on RAS effector signaling and therapy response to tyrosine kinase inhibitors.

Materials and Methods

Whole-genome exome sequencing and TITAN analysis

The plexiform neurofibroma from which the MPNST originated was large, extending across the chest wall (Supplementary Fig. S1A). We sampled a grossly distinct region that was 5 cm adjacent to the visible origin of the MPNST. The specimens were analyzed by a board-certified pathologist (V. Khachaturov) to confirm diagnosis, percent content, and viability. Extracted DNA samples for both human and mouse were prepared using Agilent SureSelect library prep with the Agilent SureSelect Human All Exon V5 and Agilent SureSelectXT2 exome capture systems, respectfully. Both human and mouse exome samples were sequenced with 2 × 100 bp reads on the Illumina HiSeq 2500 from the Michigan State University Research Technology Support Facility (MSU-RTSF) with a total mean read coverage of 50× to 90× and 15× to 20×, respectively. Read quality was assessed using FASTQC (http://www.bioinformatics.bbsrc.ac.uk/projects/fastqc/) and trimmed using seqtk (https://github.com/lh3/seqtk). After trimming, reads were mapped to the hg19 genome using BWA-MEM v 0.7.12 (http://arxiv.org/abs/1303.3997), and duplicates were removed with Picard MarkDuplicates (http://broadinstitute.github.io/picard/). Variant calling using the deduplicated BAMs was completed using GATK Best Practices with suggested default values (22–24). Somatic variants were identified using MUTECT2 (25) using default settings. Copy number alterations of MPNST samples were assessed using TITAN (26) for pre, post, and recurrent samples compared with blood exome. Default ploidy values were set to two and converge parameters were set to default values. Segment calls generated by TITAN were used for both genome wide and inferred gene-specific copy number alteration analyses.

Development of NF1-MET, NF1-P53, and NF1 mice

$Nf1^{fl/ko}$;*lox-stop-lox*$MET^{tg/+}$;*Plp-creERT*$^{tg/+}$ mice and controls were created to examine the combination of conditional *Nf1* LOH (27) with overexpression of a chimeric *Met* transgene (28, 29). These two genetic events were targeted to occur in myelinating cells immediately after birth using a tamoxifen-inducible *Plp-creERT* transgene (18) in mice with a global, constitutive mutation of the other allele of *Nf1*. $Nf1^{fl/+}$ mice were obtained from the NCI Frederick repository. $Nf1^{ko/+}$ mice were created by breeding $Nf1^{fl/+}$ mice to *CMV-Cre* mice (30). Only second generation or later $Nf1^{ko/+}$; *Cre*-negative animals were used for subsequent breeding. *Plp-creERT* (B6.Cg-Tg(Plp1-cre/ERT)3Pop/J) and *CMV-Cre*(BALB/c-Tg(CMV-cre)1Cgn/J) transgenic mice were obtained from The Jackson Laboratory. $Nf1^{fl/ko}$;*lox-stop-lox*$MET^{tg/+}$;*Plp-creERT*$^{tg/+}$ mice were produced by crossing $Nf1^{fl/fl}$;*Plp-creERT*$^{tg/+}$ mice with $Nf1^{ko/+}$;*lox-stop-lox*$MET^{tg/+}$ mice. Lactating dams were dosed with 100 μL of 20 mg/mL tamoxifen (Sigma) in corn oil (Acros Organics) by oral gavage twice daily on

postnatal days 1 to 5, based on similar previous studies (19). Of note, crosses using *Nf1*$^{fl/fl}$;*Plp-creERT*$^{tg/tg}$ mice did not yield pups at expected Mendelian ratios and were not used for this study. Nf1$^{ko/+}$ mice were created by breeding *NF1*$^{fl/+}$mice to mice carrying a *CMV-Cre* transgene. Only second-generation or later *Nf1*$^{ko/+}$; *Cre*-negative animals were used for subsequent breeding. *Nf1*$^{ko/+}$;*TP53*$^{ko/+}$ mice were created by breeding *Nf1*$^{ko/+}$ mice to 129S4-*Trp53*^{tm2Tyj}/Nci mice (functionally *TP53*$^{ko/+}$; ref. 31). All *Nf1*$^{ko/+}$;*Trp53*$^{ko/+}$ mice produced were bred to wild-type animals to confirm *cis*-conformation of *Nf1* and *Trp53* as performed in Vogel and colleagues (32). Mice producing at *Nf1*$^{ko/+}$;*Trp53*$^{ko/+}$ offspring when bred to wild types were used as founders. All animal experimentation in this study was approved by the Van Andel Institute's Internal Animal Care and Use Committee. Details on mouse genotyping procedures are in Supplementary Data.

Mouse genotyping

Tail biopsy DNA was prepared at the time of weaning using 25 mmol/L NaOH and 100 μmol/L EDTA at 95°C for 20 minutes. Additional DNA was extracted from tail biopsy, tumors, and sciatic nerve tissue at necropsy when possible using DirectPCR reagent (Viagen) according to the manufacturer's instructions. Primers used were as follows: *Met* transgene (amplicon size = 320 bp) 5′ CCT ACA GCT CCT GGG CAA CG 3′ and 5′CCA TTC GCC ATT CAG GCT GCG 3′; *Met* transgene recombined allele (420 bp) 5′ CCT ACA GCT CCT GGG CAA CG 3′ and 5′ TGG CTT TGC TGC TGC AGT CCC 3′; *Nf1* wild type (480 bp) 5′ CTT CAG ACT GAT TGT TGT ACC TGA 3′, 5′ ACC TCT CTA GCC TCA GGA ATG A 3′, *Nf1* flox (350 bp) 5′ CTT CAG ACT GAT TGT TGT ACC TGA 3′, 5′ TGA TTC CCA CTT TGT GGT TCT AAG 3′; *Nf1* recombined (280 bp) 5′ CTT CAG ACT GAT TGT TGT ACC TGA 3′, 5′ CAT CTG CTG CTC TTA GAG GAA CA 3′; and *Plp-CreERT* transgene (300 bp) 5′ CAT GTT TAG CTG GCC CAA ATG TTG CTG 3′, 5′ CGA CCA TGC CCA AGA AGA AGA GGA AGG 3′.

Development of murine MPNST tumorgrafts and drug treatment

Immediately following euthanasia of tumor-bearing mice, 15 to 25 mg portions of each tumor were transplanted into the flank of athymic nude mice using a 10 gauge trochar. Mice were examined weekly and euthanized when the tumor size exceeded 1,500 mm^3. For treatment studies, bulk tumor pieces were transplanted subcutaneously into athymic nude female mice, and tumor growth was evaluated twice weekly. When tumor volume reached approximately 150 mm^3, mice were randomized into treatment groups and dosed for 3 weeks or until mice reached euthanasia criteria. Respective doses across all treatment combinations were capmatinib (3, 10, 30 mg/kg twice daily oral gavage) and trametinib (1 mg/kg daily via oral gavage). Specific combination studies were performed with capmatinib (30 mg/kg) and trametinib (1 mg/kg) obtained from Novartis. The tumors were measured twice weekly using a caliper, and the tumor volumes were calculated as length × width × depth. A minimum of 3 tumors from each genetically engineered mouse model (GEMM) were assessed. Representative experiments are shown.

FISH

Tumor touch preps were prepared by imprinting slightly thawed tissues onto glass slides and air drying. The slides were fixed in methanol/acetic acid (3:1) for 20 minutes, equilibrated in 2× saline/sodium citrate (SSC) at 60°C for 45 minutes, digested with 0.005% pepsin at 37°C for 10 minutes, and washed with 1× PBS for 5 minutes. Slides were placed in 1% formaldehyde for 10 minutes at room temperature, 1× PBS for 5 minutes, and dehydrated in an ethanol series (70%, 85%, 95%) for 2 minutes each. Slides were denatured in 70% formamide/4× SSC at 73°C for 5 minutes, washed in a cold ethanol series (70%, 85%, 95%) for 2 minutes each, and air dried. Probes were denatured at 73°C for 5 minutes, added to the slide, and hybridized overnight at 37°C. Posthybridization washes were with 2× SSC at 73°C for 2.5 minutes, cooled in 4× SSC/0.1% Tween 20, and rinsed in H_2O. Slides were air dried and then counterstained with anti-fade DAPI. BAC clones RP23-416H6 and RP23-73G15 (located within A2 of chromosome 6) were labeled with Orange-dUTP (Abbot Molecular), BAC clone RP23-125O3 (located within A2 of chromosome 5) was labeled with Red-dUTP (Abbot Molecular), and the *Met* transgene targeting construct (containing 5.3 kb of the endogenous *Rosa26* gene and 12 kb of the combined Rosa26-targeted mouse/human *Met* transgene locus) was labeled with Green-dUTP (Abbot Molecular) using nick translation. Clone RP23-151I21 (located within A1 of chromosome 8) and clone RP23-23D5 (located within B3 of chromosome 16) were labeled with either Spectrum Green or Spectrum Orange depending on the comparison. Image acquisition was performed with a CCD camera (VDS, voss Kuhler Gmbh.) mounted on an Olympus BX51 epifluorescence microscope using FISHView software version 2.1 (Applied Spectral Imaging). Hybridization signals were scored for at least 200 nuclei per slide.

Histopathology

Mouse tissues were fixed in 10% neutral-buffered formalin for 72 hours (Thermo Fisher Scientific) and decalcified, when necessary, in Immunocal (Decal Chemical Corp) for 24 to 72 hours prior to paraffin embedding and sectioning for histology and IHC. IHC was performed on formalin-fixed paraffin-embedded samples using a citrate-based antigen retrieval system (Vector Labs). Samples were stained for MyoD (1:200, Dako Cytomation) and S100 (1:500, Dako Cytomation). Tumors were analyzed by a sarcoma pathologist (D.M. Cardona) who was blinded to the genotype of the animals. MPNST tumors demonstrated fascicular growth patterns of spindle cells that were MyoD negative. RMS tumors were spindle shaped, MyoD-positive tumors that contained more rounded cells. IHC for Ki-67 (Spring Biosciences), phosphorylated MET (Cell Signaling Technology, D26), and phosphorylated MAPK (Cell Signaling Technology, 9101) were performed using a Ventana autostainer, and images were obtained with an Aperio Digital Imaging system (Leica) and an Eclipse 55i microscope (Nikon). For the NF1-MET, NF1-P53, and NF1 models, all derived cell lines, primary tumors and tumorgrafts were characterized for consistency of the MPNST immunophenotype (IHC) and genetic alterations (FISH), and throughout serial passaging. With respect to the *in vitro* and *in vivo* experiments, one primary GEMM tumor per model was analyzed.

Western blotting

Whole-cell lysates were collected in a RIPA buffer containing protease/phosphatase inhibitor cocktail (Roche). Mouse-derived cell lines were grown to 90% confluency overnight by seeding plates with 50,000 to 75,000 cells. Cells were then serum starved for 24 hours and then treated with capmatinib for 2 hours followed by 100 ng/mL of HGF for 15 minutes. Cells were then washed with PBS and harvested in RIPA buffer plus protease

inhibitor cocktail (Roche). Lysates (20 μg) were resolved on a 4% to 20% TGX SDS-PAGE gel (Bio-Rad) and transferred to a PVDF membrane (Invitrogen). After blocking for 1 hour with 5% non-fat dry milk in TBST buffer (20 mmol/L Tris-HCl pH 7.4, 150 mmol/L NaCl, 0.1% Tween-20), blots were probed overnight at 4°C with the following primary antibodies from Cell Signaling Technology: Met (25H2; #3127), pMET (D26; #3077), AKT (#9272), pAKT (S473; #9271), MAPK (#9102), pMAPK (Thr202/Tyr204; #9101), and β-tubulin (#2146). Blots were reacted with peroxidase- conjugated antibody for 1 hour (Cell Signaling Technology) and visualized using ECL detection (Amersham).

Statistical analysis

Kaplan–Meier curves were used to display tumor-free survival and, after verifying the proportional hazards assumption, Cox regression with false discovery rate (FDR)–adjusted contrasts were used to test for differences in tumor incidence rates between mouse lines. Three mice euthanized due to hindlimb paralysis had evidence of small paraspinal neoplasms at necropsy and were therefore included as tumor events. Genotypes with no tumor events are not shown. Logistic regression with FDR-adjusted contrasts was used to test for differences in the frequencies at which the different mouse lines were euthanized or died early due to tumor burden. Linear mixed-effects models, with random slopes and intercepts, and FDR-adjusted contrasts were used to estimate and compare tumor growth rates between different capmatinib dosages within each line and between the different mono and combo therapies. Fiellers theorem with Bonferroni-adjusted significance level was used to estimate the confidence intervals for the percent reduction in tumor growth rates for mice treated with capmatinib, trametinib, or both; relative to vehicle. All analyses were conducted using R v3.2.2 (https://cran.r-project.org/) with an assumed level of significance of $\alpha = 0.05$.

Study approval

Tissue samples were collected in accordance with US Common Rule after Institutional Review Board approval at both Spectrum Health and the Van Andel Institute (Grand Rapids, MI). Written informed consent was obtained from study participants prior to inclusion in the study.

Results

Longitudinal genomic analysis of MPNST progression confirms evolving structural and sequence variations

To investigate the genomic alterations that occur during MPNST progression, we followed the disease course of an NF1-affected adolescent male who developed a high-grade, metastatic MPNST arising from a chest wall plexiform neurofibroma. Exome sequencing was performed on biopsies procured throughout disease progression: benign plexiform neurofibroma → MPNST pretreatment → MPNST posttreatment → MPNST metastasis (Fig. 1A; Supplementary Fig. S1A–S1C). The patient initially presented at 15 years of age with a rapidly enlarging mass in his left axilla that measured 11 × 9 × 17 cm by MRI (Fig. 1B, left). Biopsies were performed at diagnosis, which verified the presence of a high-grade MPNST arising within a plexiform neurofibroma (AJCC stage III, $T2bG_3N_0M_0$). The patient received neoadjuvant chemotherapy consisting of 3 cycles of ifosfamide and doxorubicin. To enhance the resectability of the tumor following neoadjuvant chemotherapy, the patient received 5,000 cGy of preoperative radiation concurrently with two further cycles of ifosfamide. The combined radiation and chemotherapy reduced the size of the tumor enough to permit wide resection with chest wall reconstruction 4 months after diagnosis (Fig. 1B, middle). Following resection, the patient completed two additional cycles of chemotherapy with ifosfamide and doxorubicin. Surveillance imaging obtained 4 months after the end of therapy revealed recurrent disease in both lungs (Fig. 1B, right) and CT-guided biopsy confirmed the diagnosis of metastatic MPNST. The recurrence was not amenable to resection, and the patient succumbed to disease 2 years from the date of original diagnosis.

To evaluate the genomic alterations that occurred during MPNST progression in this case, tumor DNA was analyzed using a shotgun whole-exome sequencing approach. Copy number alterations were inferred using TITAN with the patient's peripheral blood DNA serving as a normal control. The genomic alterations that were identified in each stage of MPNST progression are summarized in a Circos plot (Fig. 1C). No copy number alterations were found in the plexiform neurofibroma (ring a, Fig. 1C), but the pretreatment MPNST demonstrated chromosomal amplifications (orange regions) on chromosomes 1, 7, and 8 (ring b, Fig. 1C). Additional structural alterations and site-specific amplifications accumulated throughout the course of treatment (ring c, Fig. 1C). Regional amplifications on chromosome (chr) 5, chr15, a potential whole chromosomal amplification of chr7, and deletion of chr16 (ring d, Fig. 1C) developed in the metastatic lesion, specifically. Several deletions (green) were also identified in the MPNST, including a region of chr17q that contains *TP53* and *NF1*. Notably, the deleted regions of chr17q as well as regions on chr3, chr6, and chr16 progressively expanded throughout disease progression.

Focused analysis of known MPNST-related loci *AEBP2*, *CDKN2A*, *CDKN2D*, *CHD4*, *EED*, *EGFR*, *EPC1*, *EZH2*, *HGF*, *MET*, *NF1*, *PTEN*, *RASSF1*, *SUZ12*, and *TP53* was performed (Fig. 2A). The *SUZ12* locus was found to be altered in the plexiform neurofibroma, within a genomic segment that although diploid, is representative of a near LOH event on chromosome 17. Somatic mutations in *SUZ12* were not observed, but a single germline intron variant was identified. Therefore, the near LOH is representative of a potential genomic structural change within the *SUZ12* region of chromosome 17. The observed structural alterations appear to be nonrandom and favor gain of oncogenic receptor tyrosine kinases and loss of *TP53*. Balanced copy number gains in *MET*, *HGF*, and *EGFR* were noted in the pretreatment sample and preceded other sites of additional oncogene amplification or tumor suppressor loss apart from the *TP53*, *SUZ12*, and *CDKN2D* alterations, which were also present. The number of amplified *MET*, *HGF*, and *EGFR* loci was increased in the recurrent specimen (Fig. 2B). More specifically, the copy numbers of *MET*, *HGF*, and *EGFR* progressed from a balanced conformation relative to ploidy state in the pretreatment MPNST, to an imbalanced amplification above regional ploidy state in the recurrent MPNST (Fig. 2A and B). *MET* copy number gain was confirmed in MPNST specimens using quantitative copy number PCR (Supplementary Fig. S1D). Loss of *NF1* and *TP53* was also observed in the pre-, post-, and recurrent MPNST samples (Fig. 2A and B). Interestingly, the nonsynonymous coding alteration in the *TP53* gene, NC_000017.11:g.7673223G>C, was found to be present in combination with *TP53* hemizygosity in all stages of the MPNST. A similar phenomenon was observed for

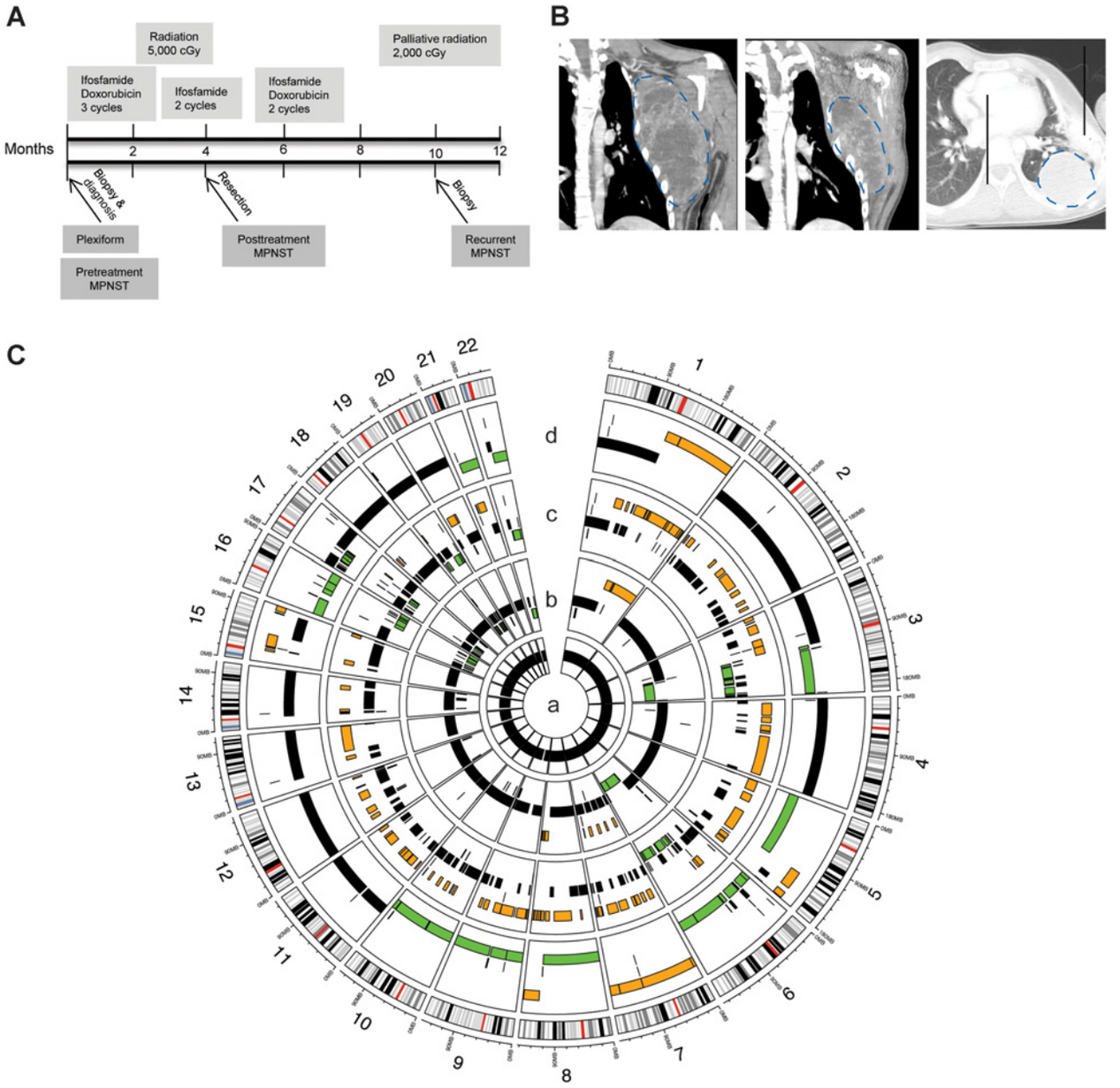

Figure 1.

Comprehensive, longitudinal genomic analysis demonstrates targetable genetic changes early in disease progression. **A,** Timeline with treatments (top) and biopsy samples (arrows, bottom; $n = 1$ sample/time point) from an MPNST and associated plexiform neurofibroma in an adolescent male with neurofibromatosis type I. **B,** The MPNST (indicated by blue dotted line) progression was imaged by MRI at diagnosis (left) and posttreatment (middle). The recurrence was imaged by computerized axial tomography (right). **C,** Summary of genomic copy number changes across the four tumor samples. The plexiform neurofibroma (inner ring, a) was genomically normal. Increased copy number gains (orange), and deletions (green) throughout the progression of the pretreatment MPNST (ring b), posttreatment MPNST (ring c), and recurrent MPNST (ring d).

a synonymous coding mutation at the hemizygous *CDKN2A* locus in the metastatic tumor. Copy-neutral LOH events were observed in the posttreatment sample in the genes *CHD4*, *EED*, *EPC1*, *PTEN*, and *RASSF1*. These observations demonstrate that copy number alterations in *MET*, *HGF*, and *EGFR* expanded from the time of diagnosis to metastasis. Whether these copy number alterations were due to DNA-damaging therapy or a defined growth advantage is unclear.

In addition, our genomic analysis revealed a substantial amount of structural variation in multiple chromosomes in the posttreatment and recurrent samples (Fig. 1C, ring c and d). The plexiform neurofibroma had very few regions of allelic imbalance and contained one predominant clonal cluster, whereas the pre-, posttreatment, and recurrent tumor samples contained large chromosomal regions of allele imbalance and additional subclonal clusters, corresponding to the genomic

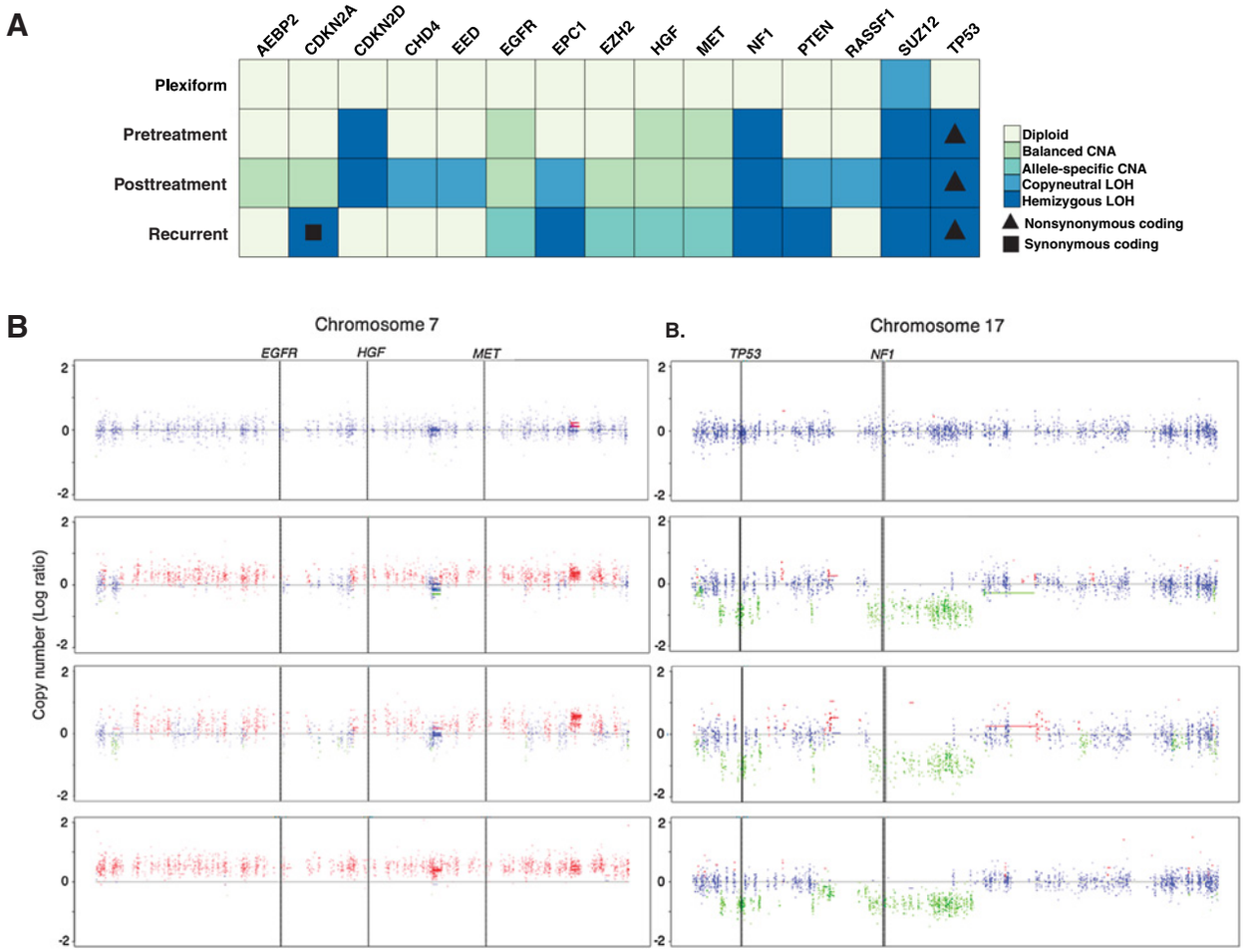

Figure 2.

Gain of *MET*, *HGF*, *EGFR*, and loss of *NF1* and *TP53* copy number observed during MPNST progression. **A,** Detailed assessment of copy number changes in known MPNST-related genes with overlaid sequence alteration data identified allele-specific copy number amplifications (CNA), balanced copy number amplifications, copy-neutral LOH, and hemizygous LOH. Triangles indicate a nonsynonymous coding change in *TP53* (NC_000017.11:g.7673223G>C). **B,** TITAN copy number analysis of variants found between blood and MPNST samples for each stage of progression was performed on chromosome 7 (**A**) and chromosome 17 (**B**). Blue, neutral; green, hemizygous LOH; red, gain. ($n = 1$ sample/time point).

aberrations (Supplementary Fig. S2). This effect is not attributable to sample necrosis as our specimens passed quality control measures for tissue viability (>99%) and DNA purity (>90%). Although some of the structural rearrangements we observed likely resulted from DNA-damaging chemotherapy and radiation treatment, the underlying clonal makeup changed over time (Supplementary Fig. S2A–S2D). For example, we observed a *CDKN2D* deletion in the pretreatment and posttreatment specimens, but not in the recurrent tumor (Fig. 2A). This suggests that the pre- and posttreatment tumor samples contained a majority cell population harboring a *CDKN2D* DLOH event (chr19), but a small subpopulation was diploid at the *CDKN2D* locus that later emerged in the recurrent tumor (Supplementary Fig. S2C and S2D; Fig. 2A). With our exome sequencing approach, it was not possible to characterize subpopulations in a detailed manner; however, our global clonality assessment indicates probable subclonal evolution over the course of disease progression.

Met amplification and *NF1* loss in peripheral nerve myelinating cells are sufficient to induce MPNST formation

To interrogate the role of MET activation in NF1-related MPNSTs, we developed a mouse model that reflects *MET* amplification in the context of *NF1* deficiency. In this *Cre*-inducible mouse model (Fig. 3A), a chimeric *Met* transgene that was previously shown to activate Met signaling above physiologic thresholds in neuronal tissue (28, 29) was combined with *Nf1* deficiency in myelinating Schwann cells (18). These two genetic events were induced immediately after birth using a tamoxifen-inducible *Plp-creERT* transgene (33) in mice with a global, constitutive loss of the *Nf1* allele. Tamoxifen induction at postnatal days 1 to 5 was selected to best replicate plexiform neurofibromagenesis based on previous studies of $Nf1^{fl/ko}$;$Plp\text{-}creERT^{tg/+}$ mice (18, 19). Allele-specific PCR confirmed recombination of the *loxp*-flanked *Nf1* gene in peripheral nerves and the presence of the recombined *Met* transgene (Fig. 3B). For brevity, we refer to the $Nf1^{fl/ko}$;$lox\text{-}stop\text{-}loxMet^{tg/+}$;$Plp\text{-}creERT^{tg/+}$ mice as "NF1-MET" mice

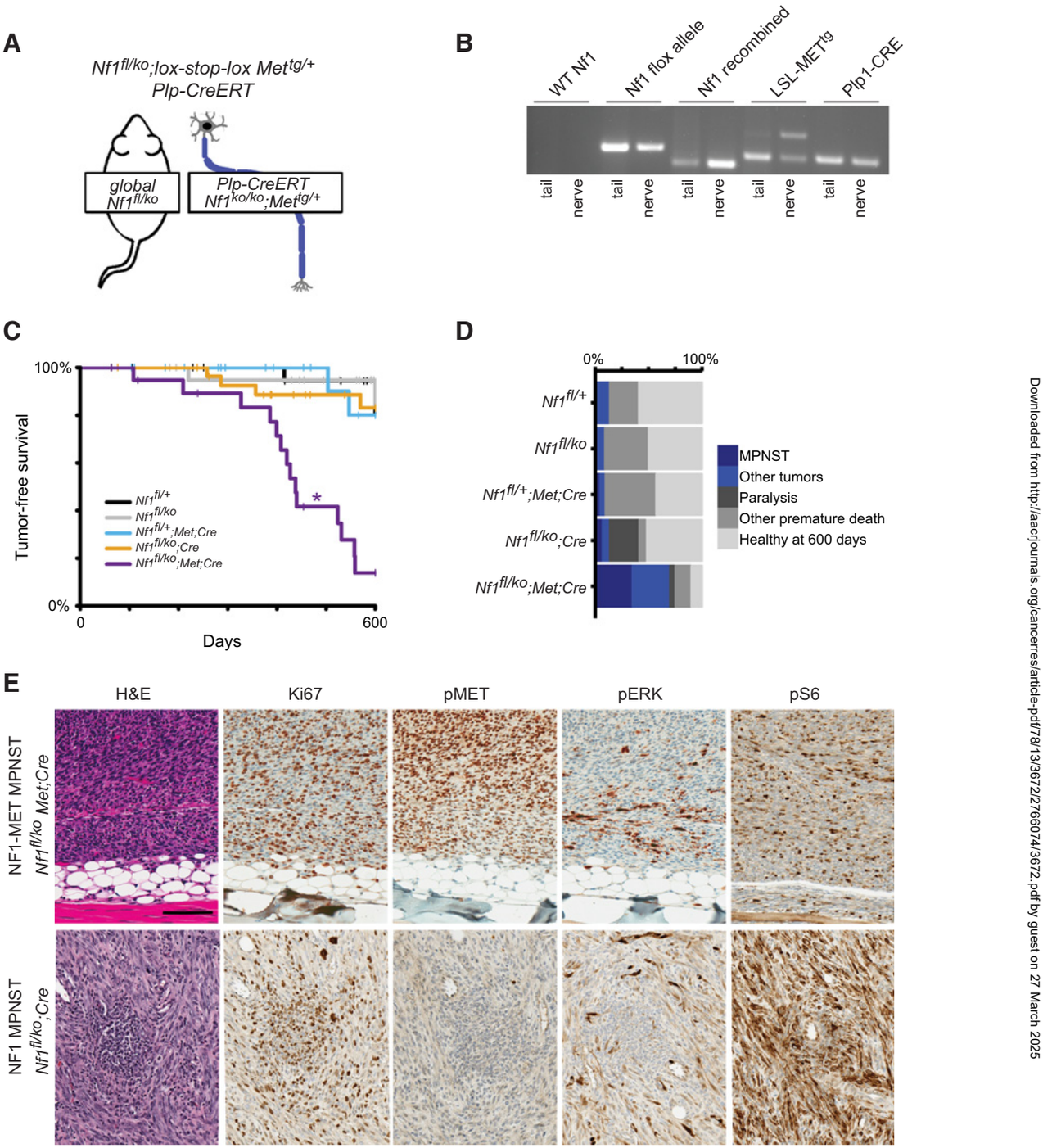

Figure 3.

MET activation drives malignant tumorigenesis in a mouse model of NF1-related MPNST. **A,** Schematic of mouse genetics. Mice have a global loss of one *Nf1* allele and loss of the second copy of *Nf1* plus activation of a *MET*-overexpressing transgene in myelinating cells following tamoxifen-induction of *Plp1-Cre/ERT* activity at postnatal day 1 to 5. **B,** Allele-specific PCR for a mouse with the combined *Nf1* loss and *MET* overexpression genotype shows absence of an unaltered *Nf1* allele (wild-type *Nf1*) and presence of the functional but *loxp*-flanked *Nf1* allele (*Nf1* flox); the recombined, loss-of-function *Nf1 ko* allele (*Nf1* recombined); the inactive *lox-stop-lox MET* transgene (*MET tg/rec*, lower band) and the recombined *tgMET* transgene (*MET* tg/rec, upper band); and the *Plp1-Cre/ERT* transgene (Plp1-Cre). **C,** Tumor-free interval data for all models plotted as Kaplan–Meier curves. *Nf1fl/ko;Met;Cre* mice developed tumors significantly sooner than all other mouse lines (indicated by *). **D,** Cause of death in the 600-day observation period is plotted by frequency. Blue, death or euthanasia related to tumor burden; grays, healthy after 600 days or death due to other causes. **E,** Hematoxylin and eosin (H&E) staining confirmed MPNST histology (representative images shown of 6 samples assessed in triplicate). Ki67 verified high rates of proliferation. High pERK and pS6 were observed by IHC; however, high pMET was only present in the NF1-MET MPNST.

throughout the article. NF1-MET mice and controls ($Nf1^{fl/ko}$;*Cre*, $Nf1^{fl/+}$;*Met*;*Cre*, and wild-type) were aged for up to 600 days to evaluate their tumor phenotypes. The tumor-free survival of NF1-MET mice was significantly decreased relative to the other four mouse lines (all $P < 0.001$; Fig. 3C). The odds of NF1-MET mice being euthanized due to tumor burden was 14.58 times higher than $Nf1^{fl/ko}$;*Cre* mice [$P = 0.0008$; 95% confidence interval (CI), 3.51–60.59)] and 23.33 times higher than $Nf1^{fl/ko}$ ($P = 0.0008$; 95% CI, 4.1–132.9).

In total, 70% of NF1-MET mice developed neoplasms, 50% of which were MPNSTs, whereas in the 13% of control mice that developed neoplasms, none were MPNSTs (Fig. 3D). MPNSTs derived from NF1-MET demonstrated the characteristic spindle cell morphology with a fascicular growth pattern (Fig. 3E). Tumors were classified as MPNSTs according to the established GEM nerve-sheath tumor classification: grade 3, $S100^{+}$/$MyoD^{-}$ with nuclear atypia, high mitotic rate, and focal necrosis or hemorrhage (Fig. 3E; ref. 34). Paralysis or pseudo-paralysis of the hindlimbs, occurring in 8 of 29 NF1-MET mice, was another major cause of premature euthanasia (Fig. 3D, dark gray bars). Tumor initiation occurred earlier in NF1-MET mice than the other four mouse lines ($P < 0.0001$), with a median tumor-free survival time of 438 days (95% CI, 408–559). Tumors from mice with activated *Met* transgene expression demonstrated a high rate of cellular proliferation (Ki67) and greater amounts of active phospho-MET (pMET) by IHC (Fig. 3E).

To evaluate MET signaling in other genomic contexts, we isolated MPNSTs from both $Nf1^{ko/+}$;$p53^{LSL\text{-}R172H}$ and $Nf1^{ko/+}$;*Plp-creERT*$^{tg/+}$ mice. $Nf1^{ko/+}$;$p53^{LSL\text{-}R172H}$ mice (referred to as "NF1-P53") were derived by crossing the $Nf1^{KO/+}$ and $p53^{LSL\text{-}R172H}$ mice (31). These mice did not require crossing with a Cre recombinase for tumor induction, as they are essentially a $p53^{ko/+}$ model as the lox-stop-lox (LSL) cassette prevents expression of the $p53^{R172H}$ mutant. MPNST tumors from NF1-P53 mice have LOH of the wild-type *p53* allele, and we confirmed that $p53^{LSL\text{-}R172H}$ is in *cis* with *Nf1* on Chr11. As a control for *NF1* deficiency alone, we aged $Nf1^{ko/+}$;*Plp-creERT*$^{tg/+}$ mice and isolated an MPNST. For simplicity, these mouse lines are referred to as "NF1" throughout the article. Immunostaining of the NF1 MPNST showed less activated MET and ERK compared with the NF1-MET MPNST (Fig. 3E).

FISH was used to evaluate the *Rosa26*-targeted *Met* transgene, the endogenous mouse *Met* gene, and the endogenous mouse *Hgf* gene. Confirmation of the transgene was performed with a *R26-MET* probe in NF1-MET mice. In normal spleen from a NF1-MET mouse, we observed 2 to 4 copies of the *Met* transgene, and in MPNSTs, we observed 2 to 8 *Met* transgene copies (Supplementary Fig. S3; Supplementary Table S1). We also performed FISH analysis to determine whether endogenous *Met* or *Hgf* was amplified in the MPNST tumors from the various mouse lines. We did not observe any additional endogenous mouse *Met* copy number gains in NF1-MET tumors (Supplementary Fig. S4A; Supplementary Table S2). Conversely, the NF1-P53 MPNST had a gain of 2 to 6 *Met* copies in 64% of tumor cells and the NF1 MPNST had a single *Hgf* copy number gain in 13% of MPNST cells (Supplementary Fig. S3B and S3C; Supplementary Table S2). To ensure the robustness of these models, each founder and the derived tumors were sequenced to verify both induced and spontaneous mutations. Additional genomic characterization of these NF1-MET mouse tumors, as well as tumors from control MPNSTs in NF1 and NF1-P53 mice, was performed using 15× to 20× whole-exome sequencing, and variants were cross-referenced against a list of genes with demonstrated roles in MPNST disease progression. No additional functional variants were detected in the mouse models apart from the engineered genomic modifications. In summary, we observed endogenous *Met* or *Hgf* copy number gains in the NF1-P53 and NF1 tumors; however, the NF1-MET MPNSTs had 4 to 10 copies of *Met* (transgene and endogenous) and represent a novel model of *Met*-amplified NF1-related MPNSTs.

NF1-MET MPNST tumorgrafts are exquisitely sensitive to MET inhibition

Because MPNSTs often develop from MET-overexpressing plexiform neurofibromas and commonly exhibit *MET* and *HGF* gene amplifications (11, 35), we evaluated the effect of MET inhibition with the kinase inhibitor capmatinib. Capmatinib (INC280) is an oral, highly selective, and potent MET inhibitor that is well tolerated and has shown clinical activity in advanced solid tumors (36, 37). Phase I and II clinical trials are ongoing to investigate the efficacy of capmatinib in cancers, including melanoma, HCC, non–small cell lung cancer (NSCLC), glioblastoma, colorectal cancer, and papillary renal cancer. Tumorgrafts and cell lines were established in immunocompromised mice from primary MPNSTs in the NF1-MET, NF1, and NF1-P53 models. Allele-specific PCR confirmed maintenance of the recombined *Nf1* gene and *Met* transgene. Because of the variability in *Met* alleles in these models, we evaluated three different concentrations of capmatinib (3, 10, and 30 mg/kg) in each MPNST tumorgraft model (Supplementary Fig. S5). Capmatinib significantly inhibited growth in the NF1-MET tumorgrafts even at the low dose of 3 mg/kg ($P < 0.0001$), suggesting these tumors are highly MET dependent. Increasing the dose to 30 mg/kg produced a significant reduction and decreased tumor growth rate by 55 mm^3 ($P < 0.0001$; Supplementary Fig. S5A–S5C). Capmatinib treatment of NF1-P53 and NF1 MPNSTs showed variable responses among tumorgrafts harvested from the original GEMMs. In separate experiments, we observed therapy responses to 30 mg/kg capmatinib that ranged from a small subgroup of tumorgrafts (Supplementary Fig. 5B) to a statistically significant effect among an entire tumorgraft cohort (Fig. 4). These results indicate that significant intertumoral heterogeneity exists within the NF1-P53 and NF1 tumorgrafts that promote resistance to MET inhibition. In comparison, in NF1-related MPNSTs with high MET expression and activity (i.e., NF1-MET), significant efficacy of MET inhibition was consistently observed (Supplementary Fig. S5C).

Evaluating the efficacy of MET or MEK inhibition in MPNST models of *MET* amplification and *P53* loss

Our results and other TKI studies suggest targeted inhibition of multiple kinase nodes may be required to minimize response variability and abrogate bypass mechanisms of resistance (38–40). Because RAS deregulation is a hallmark of NF1-related tumors, we also evaluated the efficacy of MEK inhibition in our models (21). The recent clinical success of MEK inhibition (i.e., selumetinib) in NF1-related plexiform neurofibromas highlights the therapeutic potential of targeting MEK in NF1-related peripheral nerve tumors, such as MPNSTs (41). We used the MEK inhibitor trametinib (Mekinist), which is a reversible, highly selective, allosteric inhibitor of MEK1 and MEK2 and is FDA approved for metastatic melanoma. One of the challenges of targeting the MEK/ERK pathway is achieving high-level MEK

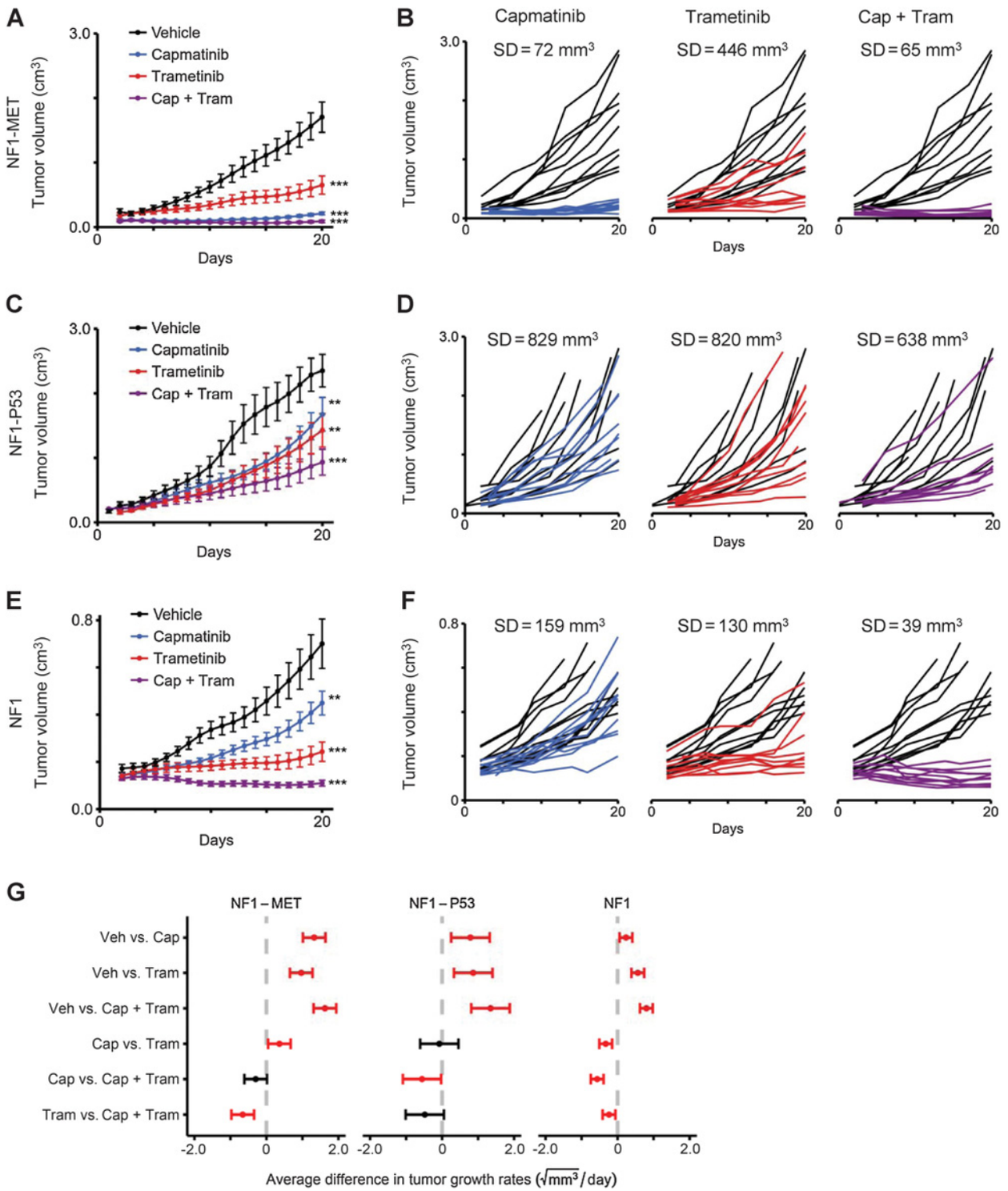

Figure 4.

Combined MET and MEK inhibition significantly decreases tumor growth and response variability. Tumor growth of NF1-MET (**A**), NF1-P53 (**C**), and NF1 tumorgrafts are plotted as means with SE (**E**). Tumor volume was imputed using last observation carried forward, until animal was euthanized. Curves terminated once >50% of mice were euthanized in the respective treatment group. Individual tumor growth for NF1-MET (**B**), NF1-P53 (**D**), and NF1 tumorgrafts (**F**) plotted by treatment (colored lines) compared with vehicle (black lines). **G,** 95% confidence intervals for the pairwise differences between the growth rates of the select treatments, estimated, and tested using linear mixed-effects models with random slopes and intercepts, and FDR adjusted contrasts. Statistically significant differences ($P < 0.05$) between compared therapies are highlighted in red. *, $P < 0.05$; **, $P < 0.01$; ***, $P < 0.001$.

inhibition without systemic toxicity. Trametinib has a strong pharmacokinetic profile with exceptional potency and specificity, oral bioavailability, and long half-life with a shallow C_{max} (peak concentration) to C_{trough} (trough concentration) profile (42). To evaluate the efficacy of MET and/or MEK inhibition in our distinct MPNST models, we measured the effect of monotherapy and combination therapy on tumor growth in the NF1-related MPNST tumorgrafts (Fig. 4). We verified our previous results and again observed exquisite sensitivity to single-agent capmatinib in NF1-MET (*P53* wild type) tumors as well as significant tumor growth inhibition with trametinib (Fig. 4A and B; $P < 1.0e^{-16}$ for both capmatinib and trametinib treatment); however, pairwise comparison revealed that capmatinib was significantly more effective than trametinib in the NF1-MET tumors ($P < 0.001$; Fig. 4G). Examining the individual growth curves for each treatment versus vehicle control groups allowed us to assess the variability in treatment response. Capmatinib treatment was associated with minimal response variability (SD = 72 mm^3), while trametinib treatment response variability (SD = 446 mm^3) was substantially higher (Fig. 4B).

In NF1-P53 tumors, we observed a more aggressive growth rate than NF1-MET and NF1 tumors (Fig. 4C and D). Both capmatinib and trametinib significantly inhibited NF1-P53 tumor growth ($P < 0.01$; Fig. 4G) in this experiment, although with both single-agent treatments, there was an aggressive growth trend after 21 days of treatment (Fig. 4C). In NF1-P53 tumors, substantial variability was observed in response to capmatinib (Fig. 4D; SD = 829 mm^3) or trametinib treatment (Fig. 4D; SD = 820 mm^3). This was in stark contrast to the homogenous response to capmatinib in the NF1-MET tumors (Fig. 4B; SD = 72 mm^3). We also evaluated the efficacy of MET and MEK inhibition in NF1 (P53 wild type) tumors, which had significantly slower growth rates compared with NF1-MET and NF1-P53 tumors and were suppressed with capmatinib ($P < 0.004$) and trametinib ($P < 1.0e-16$) treatment (Fig. 4E and F). These results indicate that NF1-related MPNSTs containing *MET* amplification are highly sensitive to MET inhibitors, yet clinical response may be further improved with the addition of a MEK inhibitor.

Combination MET and MEK inhibition is more effective than single agent regardless of P53 status

Because of the diverse bypass mechanisms of resistance to kinase inhibition, achieving a durable clinical response will likely require inhibition of multiple critical kinase signaling nodes. To compare monotherapy and combination therapy, we compared the efficacy of combined MET and MEK inhibition. In NF1-MET tumors, pairwise treatment comparisons showed that combined MET and MEK inhibition was significantly more effective than monotherapy with trametinib (Fig. 4G, $P = 0.000005$). Combination therapy in NF1-MET tumors resulted in an overall growth rate reduction of 107% compared with 89% (capmatinib) and 58% (trametinib; Supplementary Fig. S6A). Even though combination therapy of capmatinib + trametinib (65 mm^3) minimized the variability in response compared with capmatinib alone (72 mm^3; Fig. 4B), there was no significant improvement in tumor reduction with combination therapy in the NF1-MET tumors when compared with capmatinib (Fig. 4G, $P = 0.06$). These results indicate that NF1-related MPNSTs containing *MET* amplification are highly sensitive to MET inhibitors, yet clinical response may be further improved with the addition of an MEK inhibitor.

In NF1-P53 tumors, combined capmatinib + trametinib treatment significantly inhibited tumor growth ($P < 0.000002$; Fig. 4C and G) and caused a 60% growth reduction compared with monotherapy with trametinib (39%) or capmatinib (35%; Supplementary Fig. S6B). Analysis of the individual growth curves for NF1-P53 tumors revealed drastic improvement in response variability with combination therapy compared with single-agent alone (Fig. 4D and G). Capmatinib + trametinib reduced the variability in response to 638 mm^3, yet there was one "nonresponder" that impacted this variability (Fig. 4D). In pairwise comparisons, capmatinib + trametinib treatment was significantly better than capmatinib alone ($P = 0.05$) but not trametinib ($P = 0.08$; Fig. 4G). In the NF1 tumors, capmatinib + trametinib showed statistically significant improvement in tumor suppression versus single-agent therapy with either capmatinib ($P < 1.0e^{-16}$) or trametinib ($P = 0.004$; Fig. 4G; Supplementary Fig. S6C). These results indicate that NF1-related MPNSTs without *Met* amplification or *p53* loss may also be responsive to combination MET and MEK inhibition. Overall, these findings confirm that NF1-related MPNSTs with *P53* deficiency are less responsive to therapeutic approaches targeting single kinases and the best therapeutic response is achieved by inhibiting both MET and MEK signaling.

Combination MET and MEK inhibition prevents adaptive ERK and AKT response

Differential patterns of MET, RAS, and AKT signaling were observed in response to monotherapy versus combination kinase inhibition in both the *in vivo* and *in vitro* MPNST models. We examined the effect of MET and MEK inhibition on MET expression and activation (Fig. 5). As expected, capmatinib resulted in complete inhibition of MET activation in NF1-MET tumors after 2 days of treatment (Fig. 5A). NF1-MET cells produced extremely high levels of MET compared with NF1-P53 and NF1 cells, yet 5 nmol/L capmatinib completely inhibited pMET in NF1-MET MPNST cells (Fig. 5B). Despite the presence of minor *Met* amplification in NF1-P53 cells, there was no change in pMET after 2 days of capmatinib treatment in the NF1-P53 tumors (Fig. 5A). Interestingly, MET was strongly activated with trametinib treatment in the NF1-MET and NF1 tumorgrafts (Fig. 5A, trametinib column) and in the NF1-MET, NF1-P53, and NF1 cells with HGF treatment (Fig. 5C). In both the tumorgrafts (Fig. 5A) and cells (Fig. 5D), dual MET and MEK inhibition effectively abrogated pMET levels in all three MPNST models. The activation of MET following trametinib treatment was unanticipated, but suggests that feedback RTK activation occurs following RAS blockade in *NF1*-deficient cells.

To see how MET and MEK inhibition impact RAS/MEK/ERK signaling, we examined ERK activity expression in the MPNST tumorgrafts and cells. Because *NF1* deficiency results in RAS deregulation, high ERK activation was anticipated in all of the NF1-related MPNST tumors (Fig. 6A). In NF1-MET cells, ERK activation was significantly inhibited by 5 nmol/L capmatinib, whereas NF1 and especially NF1-P53 cells showed a marginal decrease in pERK in response to capmatinib (Fig. 6B). Trametinib was much more effective at inhibiting ERK activation and demonstrated reduction of pERK at 10 nmol/L in NF1-P53 and NF1-MET cells and at 5 nmol/L in NF1 cells (Fig. 6C). Combined capmatinib + trametinib treatment resulted in a greater than 90% reduction in pERK in all of the MPNST models (Fig. 6A, right). In the MPNST cells, combined capmatinib and trametinib treatment

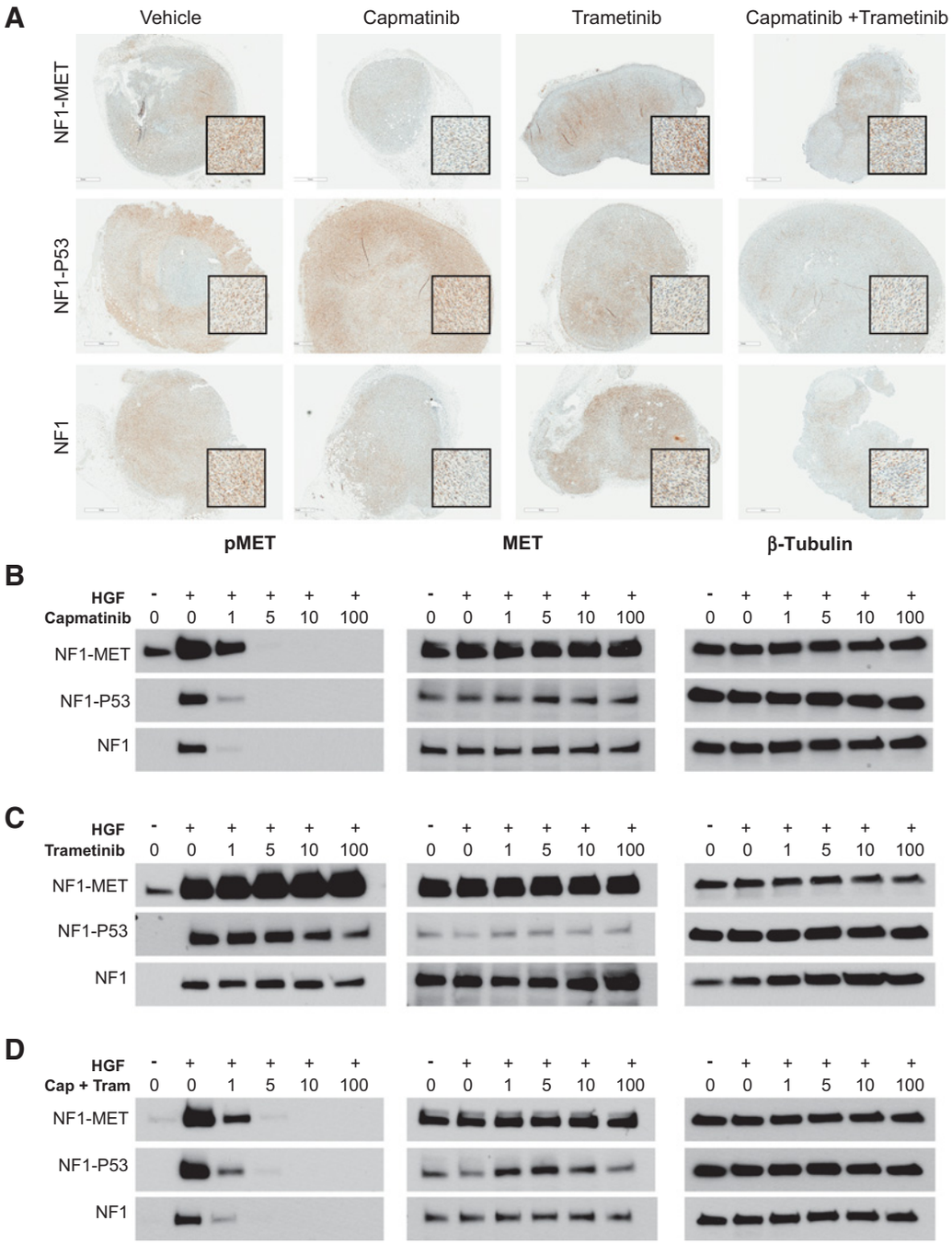

Figure 5.

Effects of MET and MEK inhibition on MET activation in NF1 MPNST models. **A,** Immunostaining of pMET (Y1234/1235) in MPNST models that were treated with kinase inhibitors for 2 days (areas of strongest signal are shown in the magnified inset boxes). **B–D,** Western blot analysis of MPNST cells treated with TKIs for 2 hours and ± HGF for pMET (left), total MET (middle), and β-tubulin control (right). The total MET exposure for the NF1-MET cells was half the time of the NF1-P53 and NF1 cells.

mirrored the tumorgraft results and was the most effective treatment in decreasing pERK (Fig. 6A and D). These findings validate the expected inhibition of RAS/ERK signaling with MEK TKIs and emphasize the importance of combined kinase inhibition to eradicate RAS signaling.

Another major signaling pathway that is activated by MET and known to interact with RAF is the PI3K/AKT pathway. We observed high pAKT at the invasive edges of the NF1-P53 tumors, yet minimal pAKT was present in NF1-MET or NF1 tumors (Fig. 7A). Interestingly, increased pAKT was observed in

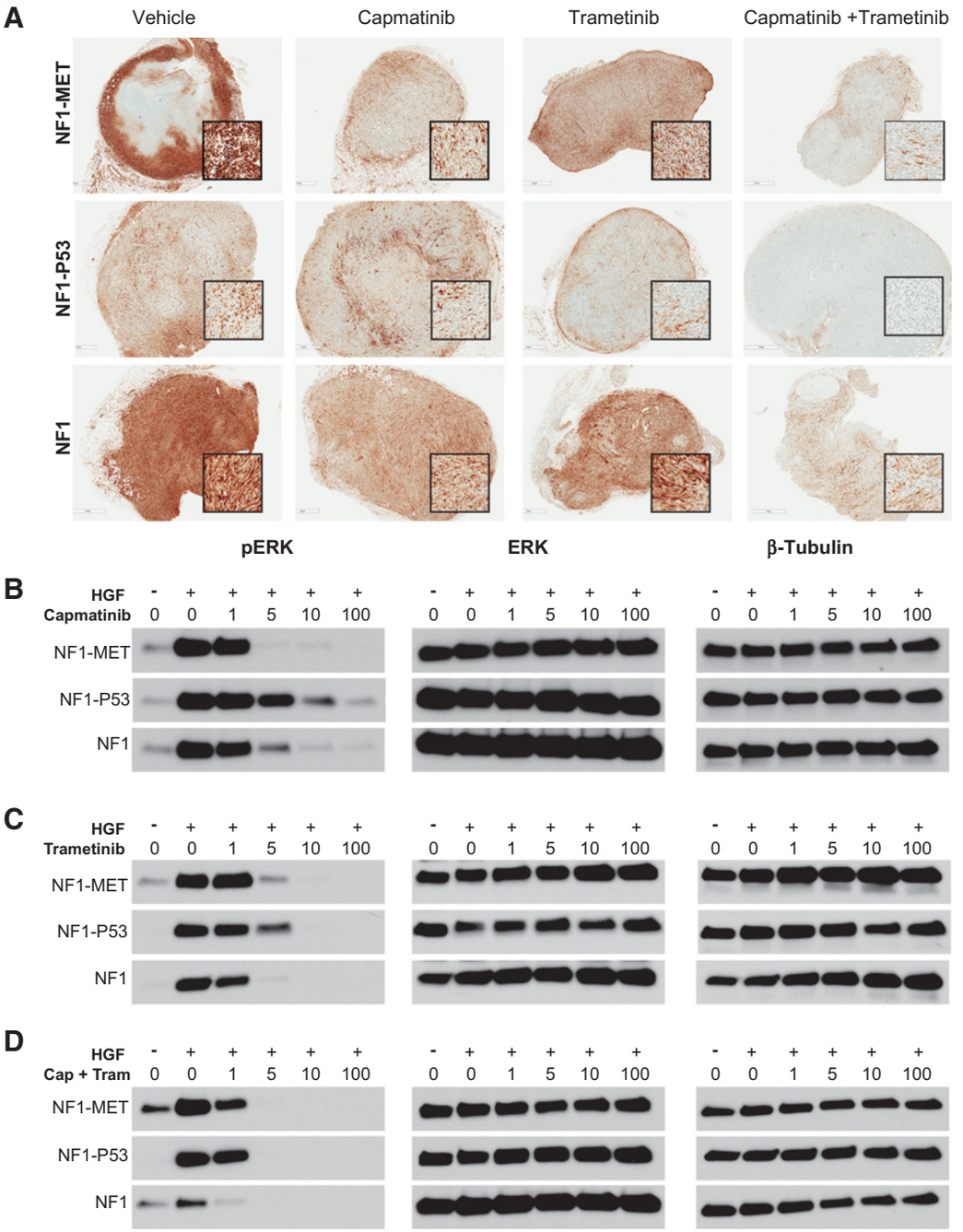

Figure 6.

Responses in ERK signaling following MET and MEK inhibition in NF1 MPNST Models. **A,** Immunostaining of pERK (T202/Y204) in MPNST models that were treated with kinase inhibitors for 2 days (areas of strongest signal are shown in the magnified inset boxes). **B–D,** Western blot analysis of MPNST cells treated with TKIs for 2 hours and ± HGF for pERK (left), total ERK (middle), and β-tubulin control (right).

NF1-P53 tumors after capmatinib or trametinib treatment and persisted at the tumor periphery even with combined capmatinib and trametinib treatment (Fig. 7A). Analysis of AKT activity in the MPNST cell lines verified our *in vivo* observations. Even though AKT expression is comparable across the MPNST lines, pAKT is significantly higher in the NF1-P53 cells at basal conditions (Figs. 7B–D). As expected, MET activation with HGF treatment stimulates pAKT in NF1-MET and NF1 cells and further augmented AKT activation in NF1-P53 cells. Capmatinib treatment resulted in a strong inhibition of AKT in NF1-MET and NF1 cells, but was ineffective in diminishing pAKT in the NF1-P53 cells (Fig. 7B). Trametinib treatment resulted in a

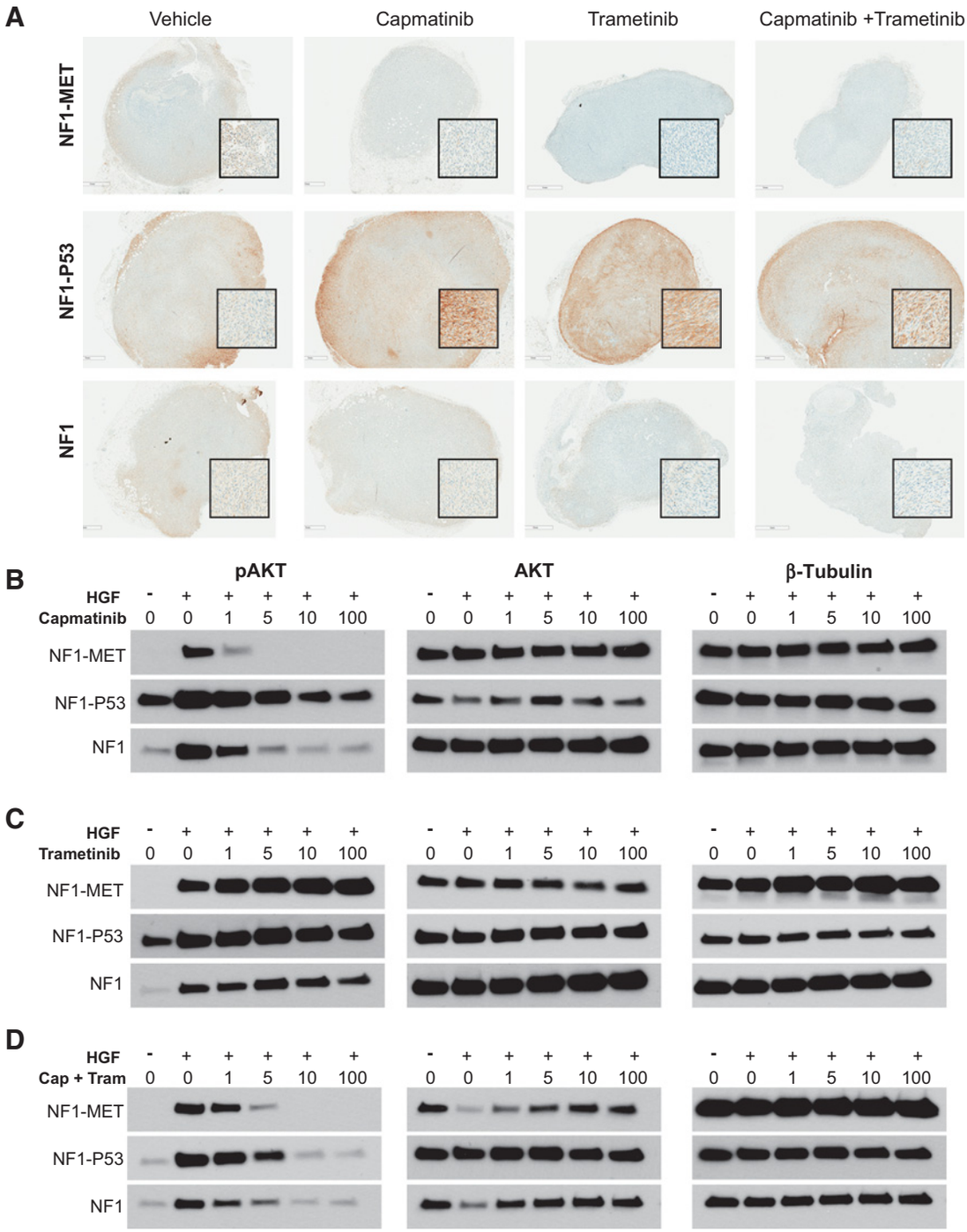

Figure 7.

Responses in AKT signaling following MET and MEK inhibition of NF1-MET, NF1-P53, and NF1 MPNSTs. **A,** Immunostaining of pAKT (S473) in MPNST models that were treated with kinase inhibitors for 2 days (areas of strongest signal are shown in the magnified inset boxes). **B–D,** Western blot analysis of MPNST cells treated with TKIs for 2 hours and ± HGF for pAKT (left), total AKT (middle), and β-tubulin control (right).

significant increase in pAKT in all three of the MPNST cells (Fig. 7C). Combined MET and MEK inhibition was the most effective treatment for abrogating AKT activation in the NF1-P53 cells (Fig. 7A and D). This analysis reveals that NF1-P53 tumors have basal AKT activity that is rapidly increased upon MET or MEK inhibition. This may indicate a distinctive mechanism of resistance that is readily activated upon kinase inhibition in *P53*-deficient MPNSTs.

Discussion

The lack of effective therapies for MPNSTs remains a significant issue for individuals affected by NF1 (2, 3). By examining the evolution of genomic alterations in the case of a single, NF1-related human MPNST, we ascertained the degree of genomic instability that occurs over the course of MPNST treatment and identified targetable drivers of disease progression in MPNSTs. Intertumoral genomic heterogeneity has been assessed in NF1-related MPNSTs (12, 20, 27, 43, 44). Somatic and structural variants that appear early and accumulate throughout disease progression represent *de facto* driver mechanisms and in the case of NF1-related MPNSTs, could indicate fundamentally important signaling pathways in Schwann cell dedifferentiation (45). In our analysis, we observed evolution of subclonal clusters that corresponded with sampling time points. In addition, we identified hemizygous microdeletions in the *NF1* and *TP53* loci in the pretreatment specimen, with concomitantly observed amplifications of *MET*, *HGF*, and *EGFR*. It is not surprising that a *TP53* variant was present in the pretreatment MPNST given the prevalence of *P53* mutations in clinical samples (46), and the driver effects of *P53* in the context of *NF1* deficiency (47); however, the early concomitant presence of *MET*, *HGF*, and *EGFR* amplifications, and the site-specific expansion of these loci over time points to an adaptive mechanism for both malignant transformation and clonal selection. The relationship between *P53* haploinsufficiency and *EGFR* amplification has been previously demonstrated in human MPNSTs (48); however, the timing and the relationship between *MET*/*HGF* and *P53* genomic status has not been evaluated. Direct cooperation between MET and RAS has been shown to promote tumor resistance in other cancers. For example, *KRAS* and *MET* amplification mediates acquired resistance to MET inhibitors in MET-addicted gastric and lung cancer cells (49). In an esophagogastric cancer patient treated with a MET inhibitor, a *KRAS* mutation was discovered as a novel cause of acquired resistance (50), whereas in KRAS-addicted cancer cells, KRAS mediated MET expression via increased MET translation and promoted "KRAS addiction" in anchorage-independent conditions (51). Given the pleiotropic effects of MET activation (10) and its emerging role in therapy resistance (52, 53), these data provide strong rationale for further exploration of MET-RAS and RAS-MET signal interactions in NF1-related MPNSTs. It should be noted that these findings were based on dependent observations in a single subject. More work is needed to determine the generalizability of these findings.

Even though therapeutically targeting RTKs has been successful in other cancers, the failure of EGFR inhibition (erlotinib) in MPNSTs indicates that other RTK pathways should be evaluated (54). To interrogate the role of MET activation in NF1-related MPNSTs, we developed a novel mouse model that reflects MET activation in the context of NF1-deficient Schwann cells. In addition to plexiform neurofibroma formation, NF1-MET mice express a robust MPNST phenotype in the absence of additional spontaneous or induced mutations. An interesting observation is that MPSNT tumorgrafts derived from NF1-P53 and NF1 mice exhibit spontaneous *Met* and *Hgf* copy number gains. Despite the presence of *Met* and *Hgf* amplifications respectively, there was no evidence of constitutive MET activation in the NF1-P53 or NF1 models, whereas the NF1-MET tumors were strongly activated without HGF stimulation. MET activation was further induced with HGF treatment in all of MPNST tumorgraft cell lines. Collectively, these data confirm that the degree of MET activation is dependent on the genomic context and that MET activation is sufficient for malignant transformation in NF1-deficient Schwann cells to MPNSTs in the setting of germline NF1 haploinsufficiency. We did not specifically assess the contribution of the tumor microenvironment to the rate of malignant transformation, but each of the models did maintain an *Nf1* haploinsufficient background at baseline.

RAS–MET signal interactions are emerging as important mechanisms of therapy resistance and disease progression. NF1-related MPNSTs are no exception, as they exhibit both *MET* and *HGF* amplifications, and deregulated RAS signaling owing to loss of *NF1*-mediated tumor suppression. The mitigated therapy response observed in other RAS-deregulated cancers following use of single-agent kinase inhibitors (i.e., EGFR inhibition in NSCLC) teaches us valuable lessons about kinome adaptation. As in *KRAS*-mutant lung cancer, it is clear that *NF1*-deficient MPNSTs also rely on functionally redundant kinome signaling networks, not just the driver effects of a single therapeutic target (39, 40, 55). We tested the efficacy of single-agent and combined inhibition of MET and MEK in MPNST models with variable levels of *MET* amplification and *P53* deficiency. We discovered that NF1-MET tumors are "MET-addicted" and extremely sensitive to capmatinib treatment. Even though NF1-MET tumors were highly sensitive to MET inhibition, response heterogeneity was decreased with combined MET and MEK inhibition. Trametinib and capmatinib significantly reduced tumor growth as single-agent therapy in both NF1-P53 and NF1 tumors. Combined capmatinib + trametinib treatment was more effective than trametinib or capmatinib alone in some of the models; however, in all tumorgrafts, combined MET and MEK inhibition reduced the response variability. Interestingly, we observed a differential pattern of kinase signaling between the *P53*-intact and *P53*-deficient models, and in response to MET and MEK inhibition. In all of the MPNST models, combined MET and MEK inhibition was the most effective treatment for decreasing ERK activity. The fact that NF1-P53 tumors have a lower basal ERK activity and a variable response to MEK inhibition suggests that P53-deficient tumors may not be exclusively dependent on RAS–ERK signaling. This idea is supported by high basal AKT activity in NF1-P53 tumors that was sustained or rapidly increased upon MET or MEK inhibition. Given that we observed increased AKT activation in response to trametinib in all of our MPNST tumor models, PI3K/AKT pathway may be a robust compensation mechanism in RAS-deregulated MPNSTs. As with ERK, combined MET and MEK inhibition was the most effective treatment for decreasing compensatory activation of AKT. Taken together, these data confirm that distinct but convergent compensation mechanisms drive resistance to capmatinib and trametinib therapy.

In conclusion, this work addresses important gaps in knowledge regarding the sufficiency of MET activation for malignant transformation of NF1-deficient peripheral nerve cells into MPNSTs, and the important role of MET activation in reinforcing RAS/ERK and PI3K/AKT signaling. These data represent the first demonstration of capmatinib treatment response in NF1-related MPNST preclinical models and support the concept that MET inhibition is a viable treatment option for the subset of MPNSTs bearing a MET-addicted

signature. Currently, it is difficult to define the size or makeup of the "MET-addicted" clinical subset in the neurofibromatosis population due to the lack of suitable biomarkers; however, MET Y1234/35 phosphorylation has been proposed as a candidate IHC marker to define MET-activated MPNSTs and predict MET inhibitor response (13). More recent data demonstrate that by combining MET phosphospecies with baseline MET receptor expression levels, better accuracy can be achieved. It is important to note that pY1234/1235 antibodies did accurately predict response to combination therapy in our models (56, 57). Our data also indicate that P53-deficient MPNSTs may have a unique signaling pattern that relies on MET and AKT signaling. Importantly, combined MET and MEK inhibitors were able to abrogate RAS/ERK and PI3K/AKT–based kinome adaptations that were observed with monotherapy. On the basis of the data presented, it is possible that MEK-targeted therapy strategies can inadvertently activate MET, resulting in broader TKI resistance. Overall, these results highlight potential therapeutic strategies treating genomically diverse MPNSTs with single-agent tyrosine kinase inhibition strategies, as well as highlight the diverse mechanisms that promote MPNST progression and therapy resistance.

Disclosure of Potential Conflicts of Interest

M.J. Bowman is a consultant/advisory board member for Michigan BioTrust for Health (Michigan Department of Health and Human Services). No potential conflicts of interest were disclosed by the other authors.

Disclaimer

The contents of this article are solely the responsibility of the authors and do not necessarily represent the official views of NTAP and JHU.

Authors' Contributions

Conception and design: J.D. Peacock, M.G. Pridgeon, M.E. Winn, C.R. Graveel, M.R. Steensma
Development of methodology: J.D. Peacock, M.G. Pridgeon, E.A. Tovar, M. Bowman, M.R. Steensma
Acquisition of data (provided animals, acquired and managed patients, provided facilities, etc.): J.D. Peacock, M.G. Pridgeon, E.A. Tovar, C.J. Essenburg, J. Grit, R.D. Dodd, M. Chen, F. Maina, R. Dono, M.R. Steensma
Analysis and interpretation of data (e.g., statistical analysis, biostatistics, computational analysis): J.D. Peacock, M. Bowman, Z. Madaj, J. Koeman, R.D. Dodd, D.M. Cardona, M. Chen, D.G. Kirsch, M.E. Winn, M.R. Steensma
Writing, review, and/or revision of the manuscript: J.D. Peacock, M.G. Pridgeon, M. Bowman, Z. Madaj, R.D. Dodd, D.M. Cardona, D.G. Kirsch, M.E. Winn, C.R. Graveel, M.R. Steensma
Administrative, technical, or material support (i.e., reporting or organizing data, constructing databases): E.A. Boguslawski, M.R. Steensma
Study supervision: M.G. Pridgeon, M.R. Steensma
Other (pathology imaging and interpretation): V. Khachaturov

Acknowledgments

We would like to thank the MSU RTSF Genomics Core for genomic analysis of the MPNST models, Patrick Dischinger for technical assistance with this study, Amanda Schuiling for assistance with statistical analysis, and Anderson Peck from the VARI Small Animal Imaging Facility for his imaging support. We would like to thank Bryn Eagleson and the VARI Vivarium for their continuous dedication. Funding for this research was made possible by the Neurofibromatosis Therapeutic Acceleration Program (NTAP), The Johns Hopkins University (JHU), and the Van Andel Institute.

The costs of publication of this article were defrayed in part by the payment of page charges. This article must therefore be hereby marked *advertisement* in accordance with 18 U.S.C. Section 1734 solely to indicate this fact.

Received October 27, 2017; revised February 8, 2018; accepted April 24, 2018; published first May 2, 2018.

References

1. Evans DG, Howard E, Giblin C, Clancy T, Spencer H, Huson SM, et al. Birth incidence and prevalence of tumor-prone syndromes: estimates from a UK family genetic register service. Am J Med Genet A 2010; 152A:327–32.
2. Porter DE, Prasad V, Foster L, Dall GF, Birch R, Grimer RJ. Survival in malignant peripheral nerve sheath tumours: a comparison between sporadic and neurofibromatosis type 1-associated tumours. Sarcoma 2009; 2009:756395.
3. Watson KL, Al Sannaa GA, Kivlin CM, Ingram DR, Landers SM, Roland CL, et al. Patterns of recurrence and survival in sporadic, neurofibromatosis Type 1-associated, and radiation-associated malignant peripheral nerve sheath tumors. J Neurosurg 2017;126:319–29.
4. Peacock JD, Cherba D, Kampfschulte K, Smith MK, Monks NR, Webb CP, et al. Molecular-guided therapy predictions reveal drug resistance phenotypes and treatment alternatives in malignant peripheral nerve sheath tumors. J Transl Med 2013;11:213.
5. Patel AV, Eaves D, Jessen WJ, Rizvi TA, Ecsedy JA, Qian MG, et al. Ras-driven transcriptome analysis identifies aurora kinase A as a potential malignant peripheral nerve sheath tumor therapeutic target. Clin Cancer Res 2012; 18:5020–30.
6. Joseph NM, Mosher JT, Buchstaller J, Snider P, McKeever PE, Lim M, et al. The loss of Nf1 transiently promotes self-renewal but not tumorigenesis by neural crest stem cells. Cancer Cell 2008;13:129–40.
7. Le LQ, Parada LF. Tumor microenvironment and neurofibromatosis type I: connecting the GAPs. Oncogene 2007;26:4609–16.
8. Varin J, Poulain L, Hivelin M, Nusbaum P, Hubas A, Laurendeau I, et al. Dual mTORC1/2 inhibition induces anti-proliferative effect in NF1-associated plexiform neurofibroma and malignant peripheral nerve sheath tumor cells. Oncotarget 2016;7:35753–67.
9. Masliah-Planchon J, Pasmant E, Luscan A, Laurendeau I, Ortonne N, Hivelin M, et al. MicroRNAome profiling in benign and malignant neurofibromatosis type 1-associated nerve sheath tumors: evidences of PTEN pathway alterations in early NF1 tumorigenesis. BMC Genomics 2013;14:473.
10. Gherardi E, Birchmeier W, Birchmeier C, Vande Woude G. Targeting MET in cancer: rationale and progress. Nat Rev Cancer 2012;12:89–103.
11. Fukuda T, Ichimura E, Shinozaki T, Sano T, Kashiwabara K, Oyama T, et al. Coexpression of HGF and c-Met/HGF receptor in human bone and soft tissue tumors. Pathol Int 1998;48:757–62.
12. Mantripragada KK, Spurlock G, Kluwe L, Chuzhanova N, Ferner RE, Frayling IM, et al. High-resolution DNA copy number profiling of malignant peripheral nerve sheath tumors using targeted microarray-based comparative genomic hybridization. Clin Cancer Res 2008;14:1015–24.
13. Torres KE, Zhu QS, Bill K, Lopez G, Ghadimi MP, Xie X, et al. Activated MET is a molecular prognosticator and potential therapeutic target for malignant peripheral nerve sheath tumors. Clin Cancer Res 2011;17:3943–55.
14. Straussman R, Morikawa T, Shee K, Barzily-Rokni M, Qian ZR, Du J, et al. Tumour micro-environment elicits innate resistance to RAF inhibitors through HGF secretion. Nature 2012;487:500–04.
15. Oddo D, Siravegna G, Gloghini A, Vernieri C, Mussolin B, Morano F, et al. Emergence of MET hyper-amplification at progression to MET and BRAF inhibition in colorectal cancer. Br J Cancer 2017;117:347–52.
16. Upadhyaya M, Spurlock G, Majounie E, Griffiths S, Forrester N, Baser M, et al. The heterogeneous nature of germline mutations in NF1 patients with malignant peripheral serve sheath tumours (MPNSTs). Hum Mutat 2006;27:716–16.
17. Miller SJ, Rangwala F, Williams J, Ackerman P, Kong S, Jegga AG, et al. Large-scale molecular comparison of human schwann cells to malignant peripheral nerve sheath tumor cell lines and tissues. Cancer Res 2006; 66:2584–91.
18. Mayes DA, Rizvi TA, Cancelas JA, Kolasinski NT, Ciraolo GM, Stemmer-Rachamimov AO, et al. Perinatal or adult Nf1 inactivation using tamoxifen-inducible PlpCre each cause neurofibroma formation. Cancer Res 2011;71:4675–85.

19. Le LQ, Liu C, Shipman T, Chen Z, Suter U, Parada LF. Susceptible stages in schwann cells for NF1-associated plexiform neurofibroma development. Cancer Res 2011;71:4686–95.
20. Cichowski K, Shih TS, Schmitt E, Santiago S, Reilly K, McLaughlin ME, et al. Mouse models of tumor development in neurofibromatosis type 1. Science 1999;286:2172–6.
21. Dodd RD, Mito JK, Eward WC, Chitalia R, Sachdeva M, Ma Y, et al. NF1 deletion generates multiple subtypes of soft-tissue sarcoma that respond to MEK inhibition. Mol Cancer Ther 2013;12:1906–17.
22. McKenna A, Hanna M, Banks E, Sivachenko A, Cibulskis K, Kernytsky A, et al. The genome analysis toolkit: a mapReduce framework for analyzing next-generation DNA sequencing data. Genome Res 2010; 20:1297–303.
23. DePristo MA, Banks E, Poplin R, Garimella KV, Maguire JR, Hartl C, et al. A framework for variation discovery and genotyping using next-generation DNA sequencing data. Nat Genet 2011;43:491–8.
24. Van der Auwera GA, Carneiro MO, Hartl C, Poplin R, Del Angel G, Levy-Moonshine A, et al. From FastQ data to high confidence variant calls: the genome analysis toolkit best practices pipeline. Curr Protoc Bioinformatics 2013;43:11 10 1–33.
25. Cibulskis K, Lawrence MS, Carter SL, Sivachenko A, Jaffe D, Sougnez C, et al. Sensitive detection of somatic point mutations in impure and heterogeneous cancer samples. Nat Biotechnol 2013;31:213–9.
26. Ha G, Roth A, Khattra J, Ho J, Yap D, Prentice LM, et al. TITAN: inference of copy number architectures in clonal cell populations from tumor whole-genome sequence data. Genome Res 2014;24:1881–93.
27. Miller SJ, Rangwala F, Williams J, Ackerman P, Kong S, Jegga AG, et al. Large-scale molecular comparison of human schwann cells to malignant peripheral nerve sheath tumor cell lines and tissues. Cancer Res 2006; 66:2584–91.
28. Fan Y, Richelme S, Avazeri E, Audebert S, Helmbacher F, Dono R, et al. Tissue-specific gain of RTK signalling uncovers selective cell vulnerability during embryogenesis. PLoS Genet 2015;11:e1005533.
29. Genestine M, Caricati E, Fico A, Richelme S, Hassani H, Sunyach C, et al. Enhanced neuronal Met signalling levels in ALS mice delay disease onset. Cell Death Dis 2011;2:e130.
30. Schwenk F, Baron U, Rajewsky K. A cre-transgenic mouse strain for the ubiquitous deletion of loxP-flanked gene segments including deletion in germ cells. Nucleic Acids Res 1995;23:5080–1.
31. Olive KP, Tuveson DA, Ruhe ZC, Yin B, Willis NA, Bronson RT, et al. Mutant p53 gain of function in two mouse models of Li-Fraumeni syndrome. Cell 2004;119:847–60.
32. Vogel KS, Klesse LJ, Velasco-Miguel S, Meyers K, Rushing EJ, Parada LF. Mouse tumor model for neurofibromatosis type 1. Science 1999;286: 2176–9.
33. Leone DP, Genoud S, Atanasoski S, Grausenburger R, Berger P, Metzger D, et al. Tamoxifen-inducible glia-specific Cre mice for somatic mutagenesis in oligodendrocytes and Schwann cells. Mol Cell Neurosci 2003;22: 430–40.
34. Stemmer-Rachamimov AO, Louis DN, Nielsen GP, Antonescu CR, Borowsky AD, Bronson RT, et al. Comparative pathology of nerve sheath tumors in mouse models and humans. Cancer Res 2004;64:3718–24.
35. Mantripragada KK, Spurlock G, Kluwe L, Chuzhanova N, Ferner RE, Frayling IM, et al. High-Resolution DNA copy number profiling of malignant peripheral nerve sheath tumors using targeted microarray-based comparative genomic hybridization. Clin Cancer Res 2008;14:1015–24.
36. Ma B, Bang YJ, Lim WT, Nam DH, Su WC, Schellens JHM, et al. P1.04Phase I dose escalation and expansion study to evaluate safety and efficacy of INC280 in patients with advanced MET-dependent solid tumors. Ann Oncol 2015;26:ii17.
37. Bang Y-J, Su W-C, Nam D-H, Lim W-T, Bauer TM, Brana I, et al. Phase I study of the safety and efficacy of INC280 in patients with advanced MET-dependent solid tumors. J Clin Oncol 2014;32:2520–20.
38. Linklater ES, Tovar EA, Essenburg CJ, Turner L, Madaj Z, Winn ME, et al. Targeting MET and EGFR crosstalk signaling in triple-negative breast cancers. Oncotarget 2016;7:69903–15.
39. Wilson TR, Fridlyand J, Yan Y, Penuel E, Burton L, Chan E, et al. Widespread potential for growth-factor-driven resistance to anticancer kinase inhibitors. Nature 2012;487:505–9.
40. Chong CR, Janne PA. The quest to overcome resistance to EGFR-targeted therapies in cancer. Nat Med 2013;19:1389–400.
41. Dombi E, Baldwin A, Marcus LJ, Fisher MJ, Weiss B, Kim A, et al. Activity of selumetinib in neurofibromatosis type 1-related plexiform neurofibromas. N Engl J Med 2016;375:2550–60.
42. Gilmartin AG, Bleam MR, Groy A, Moss KG, Minthorn EA, Kulkarni SG, et al. GSK1120212 (JTP-74057) is an inhibitor of MEK activity and activation with favorable pharmacokinetic properties for sustained in vivo pathway inhibition. Clin Cancer Res 2011;17:989–1000.
43. Spurlock G, Knight SJ, Thomas N, Kiehl TR, Guha A, Upadhyaya M. Molecular evolution of a neurofibroma to malignant peripheral nerve sheath tumor (MPNST) in an NF1 patient: correlation between histopathological, clinical and molecular findings. J Cancer Res Clin Oncol 2010;136:1869–80.
44. Castellsague J, Gel B, Fernandez-Rodriguez J, Llatjos R, Blanco I, Benavente Y, et al. Comprehensive establishment and characterization of orthoxenograft mouse models of malignant peripheral nerve sheath tumors for personalized medicine. EMBO Mol Med 2015;7:608–27.
45. Rahrmann EP, Watson AL, Keng VW, Choi K, Moriarity BS, Beckmann DA, et al. Forward genetic screen for malignant peripheral nerve sheath tumor formation identifies new genes and pathways driving tumorigenesis. Nat Genet 2013;45:756–66.
46. Hirbe AC, Dahiya S, Miller CA, Li T, Fulton RS, Zhang X, et al. Whole exome sequencing reveals the order of genetic changes during malignant transformation and metastasis in a single patient with NF1-plexiform neurofibroma. Clin Cancer Res 2015;21:4201–11.
47. Brekke HR, Kolberg M, Skotheim RI, Hall KS, Bjerkehagen B, Risberg B, et al. Identification of p53 as a strong predictor of survival for patients with malignant peripheral nerve sheath tumors. Neuro Oncol 2009;11:514–28.
48. Rahrmann EP, Moriarity BS, Otto GM, Watson AL, Choi K, Collins MH, et al. Trp53 haploinsufficiency modifies EGFR-driven peripheral nerve sheath tumorigenesis. Am J Pathol 2014;184:2082–98.
49. Cepero V, Sierra JR, Corso S, Ghiso E, Casorzo L, Perera T, et al. MET and KRAS gene amplification mediates acquired resistance to MET tyrosine kinase inhibitors. Cancer Res 2010;70:7580–90.
50. Kwak EL, Ahronian LG, Siravegna G, Mussolin B, Godfrey JT, Clark JW, et al. Molecular heterogeneity and receptor coamplification drive resistance to targeted therapy in MET-amplified esophagogastric cancer. Cancer Discov 2015;5:1271–81.
51. Fujita-Sato S, Galeas J, Truitt M, Pitt C, Urisman A, Bandyopadhyay S, et al. Enhanced MET translation and signaling sustains K-ras-driven proliferation under anchorage-independent growth conditions. Cancer Res 2015;75:2851–62.
52. Chen CT, Kim H, Liska D, Gao S, Christensen JG, Weiser MR. MET activation mediates resistance to lapatinib inhibition of HER2-amplified gastric cancer cells. Mol Cancer Ther 2012;11:660–9.
53. Turke AB, Zejnullahu K, Wu YL, Song Y, Dias-Santagata D, Lifshits E, et al. Preexistence and clonal selection of MET amplification in EGFR mutant NSCLC. Cancer Cell 2010;17:77–88.
54. Albritton KH, Rankin C, Coffin CM, Ratner N, Budd GT, Schuetze SM, et al. Phase II study of erlotinib in metastatic or unresectable malignant peripheral nerve sheath tumors (MPNST). J Clin Oncol 2006; 24:9518–18.
55. Wagner JP, Wolf-Yadlin A, Sevecka M, Grenier JK, Root DE, Lauffenburger DA, et al. Receptor tyrosine kinases fall into distinct classes based on their inferred signaling networks. Sci Signal 2013;6:ra58.
56. Huang F, Ma Z, Pollan S, Yuan X, Swartwood S, Gertych A, et al. Quantitative imaging for development of companion diagnostics to drugs targeting HGF/MET. J Pathol Clin Res 2016;2:210–22.
57. Srivastava AK, Hollingshead MG, Weiner J, Navas T, Evrard YA, Khin SA, et al. Pharmacodynamic response of the MET/HGF receptor to small-molecule tyrosine kinase inhibitors examined with validated, fit-for-clinic immunoassays. Clin Cancer Res 2016;22:3683–94.